Kobe University Repository : Kernel

PDF issue: 2025-12-05

Dynamic Symmetry Conversion in Mixed-Halide Hybrid Perovskite upon Illumination

Tominaka, Satoshi ; Karimata, Izuru ; Matsuoka, Takahide ; Sakamoto, Moeri ; Nakajima, Takahito ; Ohara, Koji ; Tachikawa, Takashi

(Citation)
ACS Energy Letters,6(11):3858-3863

(Issue Date)
2021-10-12

(Resource Type)
journal article

(Version)
Accepted Manuscript

(Rights)
This document is the Accepted Manuscript version of a Published Work that appeared in final form in ACS Energy Letters, copyright © 2021 American Chemical Society after peer review and technical editing by the publisher. To access the final edited and published work see http://pubs.acs.org/articlesonrequest/AOR-TFVCVAEE7P2A6A5CMESE.

(URL)
https://hdl.handle.net/20.500.14094/0100476411

KOBE UNIVERSITY

Dynamic Symmetry Conversion in Mixed Halide Hybrid Perovskite upon Illumination

Satoshi Tominaka,*,† Izuru Karimata,‡ Takahide Matsuoka,§ Moeri Sakamoto,‡ Takahito Nakajima,‡,§ Koji Ohara,⊥ Takashi Tachikawa*,‡,∥

†International Centre for Materials Nanoarchitectonics (MANA), National Institute for Materials Science (NIMS), ‡Department of Chemistry, Graduate School of Science, Kobe University, 1-1 Rokkodai-cho, Nada-ku, Kobe 657-8501, Japan. 1-1 Namiki, Tsukuba, Ibaraki 305-0044, Japan. §RIKEN Center for Computational Science, Kobe 650-0047, Japan. ⊥Japan Synchrotron Radiation Research Institute (JASRI), Kouto 1-1-1, Sayo-cho, Sayo-gun, Hyogo 679-5198, Japan. ∥Molecular Photoscience Research Center, Kobe University, 1-1 Rokkodai-cho, Nada-ku, Kobe 657-8501, Japan.

*TOMINAKA.Satoshi@nims.go.jp (ST), tachikawa@port.kobe-u.ac.jp (TT).

ABSTRACT: Organic–inorganic hybrid halide perovskites (ABX_3, where A = $CH_3NH_3^+$ (methylammonium ion, MA); B = Pb^{2+}; and X = Br^-, I^-, or Cl^-) have excellent optoelectronic properties and are highly efficient photovoltaic materials, but their chemical instability impedes their development for use in next-generation solar cells, wherein they serve as the light-harvesting material. Here, we propose a mechanism of photoluminescence red shift, a performance-loss phenomenon known as light-induced halide segregation, in mixed halide perovskites upon illumination using in situ single-particle spectroscopy and synchrotron-based X-ray techniques. Our experimental analyses suggest a defect-assisted photoinduced transition from ordinary nonpolar phases to polar phases at the local scale within seconds is coupled with organic cation reorientation, which in turn narrows the bandgap; first-principles calculations quantitatively supported this result. Our findings provide deeper insights into the nature of local polar domains in hybrid perovskite materials and help improve device stability and efficiency.

A power conversion efficiency (PCE) of over 25% can be achieved with organic–inorganic hybrid halide perovskites,[1,2] which can be further increased by bandgap tuning by introducing two or more halide anions under moderate synthetic conditions.[3–5] However, visible light illumination causes the segregation of halogen anions in mixed halide systems,[6] creating I-rich domains with narrower bandgaps. This leads to a large loss of voltage (by over 10%[7]) owing to charge recombination. Photoluminescence (PL) redshifts of 0.1–0.5 eV, as observed by different researchers (Table S1), are recognised as a signature of this halide segregation, but the underlying mechanism is still under debate,[6] perhaps owing to differences in the sample conditions. Furthermore, this segregation is probably triggered by ion migration at the defective surfaces and grain boundaries of polycrystalline films[8] that subsequently extends into the entire film.[9]

Here, to investigate the relationship between the crystal structure and the optical properties of halide perovskites while avoiding particle aggregation and any substrate effects, we prepared homogeneous isolated monocrystalline nanoparticles (~18 nm) of a mixed halide perovskite, $MAPb(Br_{0.5}I_{0.5})_3$ (Figure 1a). The UV-visible absorption and emission spectra of the nanoparticles (dispersed in toluene) were typical for $MAPb(Br_{0.5}I_{0.5})_3$ (Figures 1b, S1, and S2). The PL properties were investigated using widefield and confocal microscopy by depositing the nanoparticles on a cover glass and immersing them in solvent (1:1 (v/v) toluene/*n*-heptane) to avoid degradation (Figure 1c). A single nanoparticle or small aggregates of particles appeared as luminescent spots in the PL images (Figure 1d), but these spots were larger than the actual particles owing to the diffraction limit of visible light. Under 405 nm excitation (excitation intensity: 20 mW cm^{-2}), the PL intensity gradually increased over time, and the peak position shifted from 640 to 720 nm (Figure 1e). This redshift was also observed for a solvent-dispersed sample (Figure S2) and is consistent with the findings of previous studies.[10,11] The PL shift, which was reversible and depended on the excitation intensity (Figure S3), saturated in tens of seconds (Figure 1f, $k_{forward}$ = 0.066 s^{-1}), whereas the backward change was faster ($k_{backward}$ = 0.091 s^{-1}) than that for bulk crystals (6.8 × 10^{-3} s^{-1}).[11] Furthermore, the average PL decay lifetime gradually increased under illumination (Figure S4 and Table S2), indicating suppressed nonradiative recombination.[12] The PL spectra exhibited no peaks assignable to Br-rich phases (500–600 nm) (Figures 1e and S2).[13]

To further explore the mechanism of PL redshift, we measured the PL emission from individual spots over time in two wavelength regions: 574–626 nm (orange PL), originating from the as-prepared particles; and 672–696 nm (red PL), which slowly increases with a weak excitation intensity (excitation intensity: 3.5 mW cm^{-2}). As shown in Figures 2a and 2b, the red PL signals from individual nanoparticles exhibited a blinking behavior (intermittent on and off PL) during the initial stage, which is a characteristic signature of a single particle,[14] whereas the orange PL intensity gradually decreased without blinking. The independent blinking of the red PL signals suggests the formation and dissociation of emissive sites for lower-energy PL rather than the charging and discharging of nanoparticles.[15] The uncorrelated PL

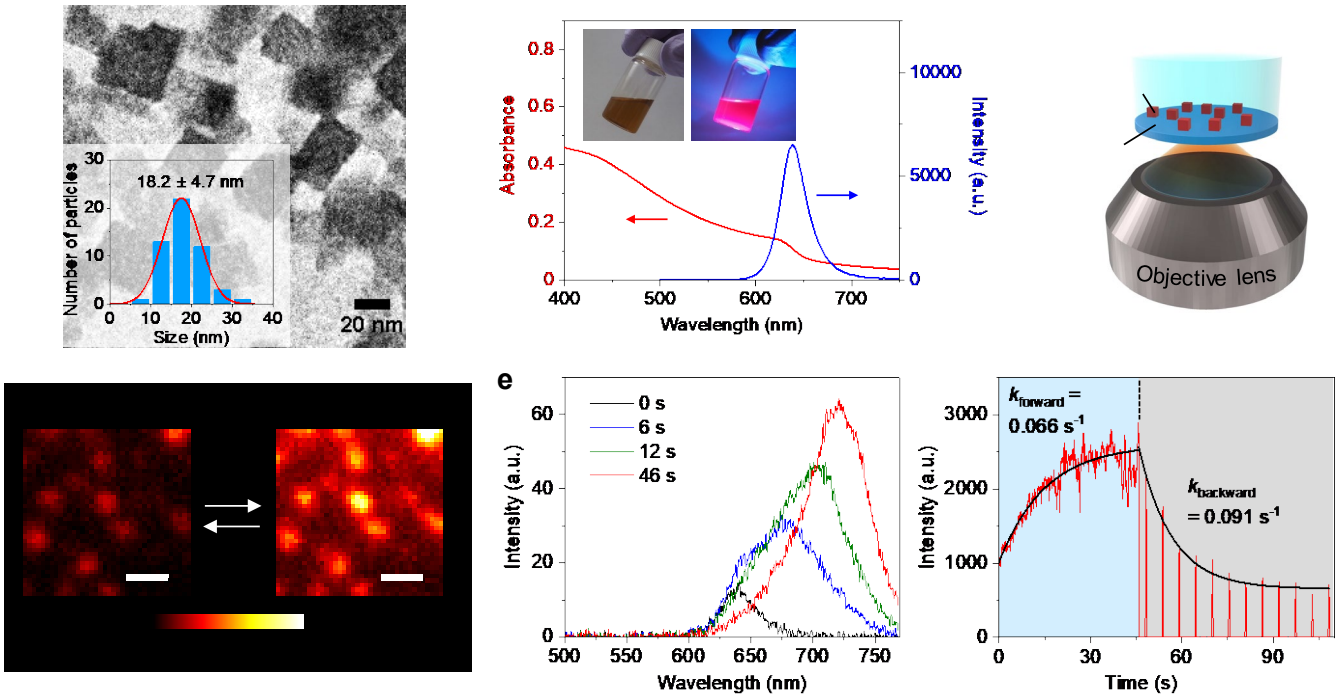

Figure 1. (a) Transmission electron microscopy image and (inset) particle size distribution. (b) UV-visible absorption and PL spectra of toluene-dispersed nanoparticles. (Insets) Photographs of the colloidal solution illuminated by visible (left) and UV (right) light. (c) Schematic of the PL microscopy measurement system. Particles were deposited on a cover glass in solvent and observed using inverted fluorescence microscopy with 405 nm laser irradiation. (d) PL images captured immediately after irradiation (left) and after sustained irradiation (right). Scale bars: 1 μm. (e) Temporal evolution of PL spectra. (f) Typical change in the PL intensity under irradiation. The backward process was traced by intermittently recording the PL spectra by flashing the excitation light.

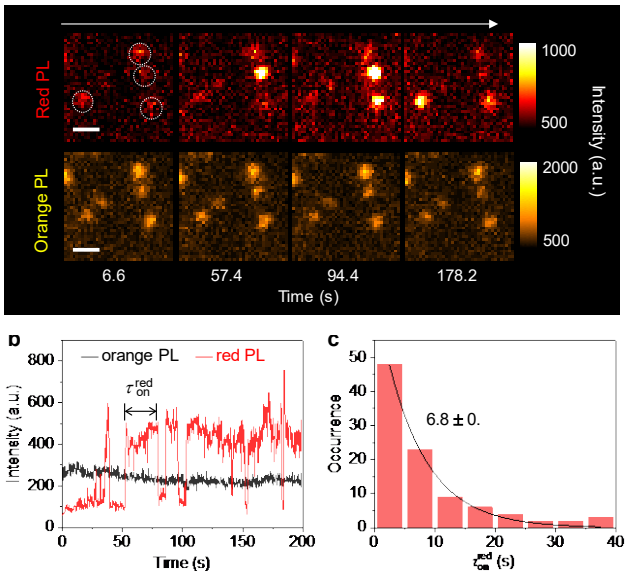

Figure 2. (a) PL images captured simultaneously using two bandpass filters under irradiation. Scale bars: 1 μm. (b) Typical intensity trajectories for a single object. (c) Histogram of on-time (τ^{red}_{on}) for bursts of red PL.

behavior can be accounted for by two possible mechanisms. (*i*) The PL intensities of two species reflect the difference in their emission efficiencies. The red-emitting species that are stochastically generated from the initial state should be only a small part of the particle. If quantum yields of the red-emitting species are much higher than those of the original orange-emitting species (approximately 0.01), as suggested by PL lifetime measurements (Figure S4 and Table S2), the corresponding PL intensity changes in the orange channel might be buried in the background. (*ii*) It is presumed that there is no direct equilibrium between the orange- and red-emitting species. If the structural transition involves non- or weakly luminescent intermediate(s), the orange PL intensity is not correlated with the red PL intensity.

As shown in Figure 2c, the probability distribution of the red PL duration time (τ^{red}_{on}) followed a single-exponential curve with a characteristic lifetime of 6.8 ± 0.5 s. Because this value is close to the reciprocal of the backward rate of change ($k_{backward}$), the increasing PL under intense excitation conditions is ascribed to the accumulation of emissive local domains with a specific lifetime. Temperature-dependent experiments (Figure S5) revealed that the integral of the PL change had an activation energy of 0.3–0.4 eV, which is close to that for halide anion migration (0.17–0.43 eV).[16] As nanoparticles embedded in the polystyrene film did not show a directional peak shift (Figure S6),[17] these PL changes are likely to be triggered by halide migration through/to anion vacancies, probably at the surface.

The structural changes upon illumination were analysed by in situ synchrotron X-ray scattering using colloidal nanoparticle dispersions, which were kept dilute to avoid coagulation (Figure 3a). The solvent signal was subtracted to

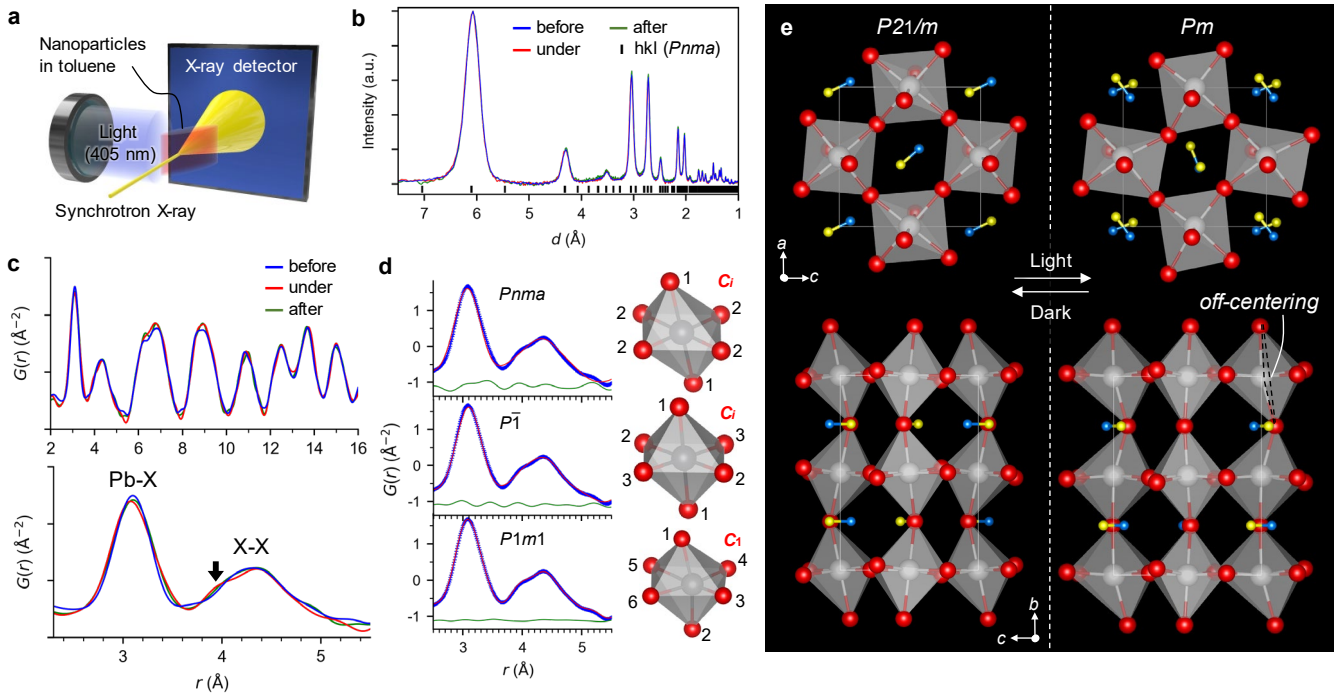

Figure 3. (a) Schematic of the data collection system. (b) XRD patterns obtained from X-ray total scattering data. (c) Pair distribution functions (PDFs) before (blue), under (red), and after (green) light irradiation with notation of nearest neighbour positions. The arrow shows the shoulders formed by illumination. (d) Left, PDF fittings using structural models in the three space groups of *Pnma*, $P\bar{1}$, and *Pm* (*P*1*m*1). The fittings were performed in the range of 1.5 to 16 Å (details are shown in the supporting information file) (Blue dots: experimental data; red curves: simulated data; green curves: difference). Right, the PbX_6 octahedra in the perovskite structures (Pb: grey; Br/I: red). The numbers are site numbers of the halogen sites. Point groups of the octahedra are also shown in red. (e) Structural models used for PDF fitting (Pb: grey; Br/I: red, N: blue; C: yellow).

obtain data for the nanoparticles (Figure S7). In the X-ray diffraction (XRD) patterns, no peak splitting was observed (Figure 3b), indicating that there was no distinct phase segregation. Peak splitting has been observed previously[10]; however, it does not always accompany PL shifts and has not been reproduced quantitatively.[16] In addition, the XRD peaks did not appear to shift drastically upon illumination.

Pair distribution functions (PDFs) reveal interatomic distances and are useful for discussing the local structure, such as PbX_6 octahedral tilts. The PDF peak (Figure 3c) associated with halide–halide (X–X) atomic pairs (3.8–5.3 Å) changes upon illumination, with a shoulder appearing at around 4.0 Å, indicating octahedral distortion.[18,19] The XRD and PDF curves were simultaneously fitted using the typical orthorhombic structural model for the space group (*Pnma: P*2$_1$/*n* 2$_1$/*m* 2$_1$/*a*). The orthorhombic lattice of the perovskite structure, wherein PbX_6 corner-linked octahedra are rotated along all three axes, simulates the experimental X-ray data well. In more details, the *Pnma* space group does not simulate details of PDF peak intensities well (Figure S8). Moreover, the shoulder at 4.0 Å found during the irradiation (Figure 3c) cannot be simulated. These are reasonable because this space group has two independent halogen sites of multiplicities of 4 and 8 (Table S3), where the halogen ions of $Br_{0.5}I_{0.5}$ are not arranged well. Thus, taking the halogen contents into account, subgroups of *Pnma* are reasonable candidates for describing the local structure.

The X-ray data were analysed by the joint refinements of PDF (local structure) and XRD (averaged structure) systematically using the maximal subgroups of *Pnma* (seven space groups) (Figures S8–31). In the joint refinements, we used the common occupancies and lattice parameters, and different atomic coordinates and atomic displacement parameters. The space groups of *P*2$_1$*ma* and *P*2$_1$/*m* can simulate the PDFs and XRD patterns well (Tables S4-6). Both the space groups lose the 2$_1$ screw axis parallel to the *c* axis and *n* glide plane (Table S3). Upon the irradiation, the structure can be simulated using the *P*2$_1$*ma* space group slightly better than *P*2$_1$/*m*. This is reasonable because the point group of PbX_6 octahedra in *P*2$_1$*ma* (*C*$_1$) is more flexible to simulate the anisotropic X-X peak behavior than of *P*2$_1$/*m* (*C*$_i$) (cf. Table S3). Such lower symmetries of octahedra were known as the cation displacement (i.e. cation off-centring in PbX_6 octahedra), which is considered to originate from lone pairs of Pb^{2+} (s^2p^0 electronic configuration).[20]

The goodness of fit parameters of the *P*2$_1$*ma* and *P*2$_1$/*m* space groups are not significantly different, and the choice of space group is not conclusive. Thus, we further analysed the local structures by the PDF fitting using subgroups of *P*2$_1$*ma* and *P*2$_1$/*m* (*P*2$_1$11, *P*1*m*1, *P*11*a*, *P*12$_1$1, and $P\bar{1}$) in order to find the minimum constraints for simulating the shoulder feature. It is apparent that the *P*1*m*1 space group is the best to represent the PDF data, in particular the shoulder was simulated well, rather than the centrosymmetric $P\bar{1}$ space group (Figures 3d, S32, S33, and Table S7). Thus, from these structural analyses, it is found that the appearance of the shoulder peak indicates formation of low-symmetric octahedra. We can summarize the structural change as the structure before irradiation, where no shoulder was found, should be in the *P*2$_1$/*m*

or a centrosymmetric structure, and it turned into the *Pm* structure by losing the inversion centres (Figure 3e).

Such formation of non-centrosymmetric structure from centrosymmetric perovskites was reported for perovskites: The $P2_1ma$ structure, which is observed for perovskite oxides (e.g. $BiFeO_3$[21]) and halide perovskites under tensile strain.[22] These properties have been used to interpret the emergence of ferroelectricity in $CdTiO_3$ upon slight lattice changes through a centrosymmetric-to-noncentrosymmetric orthorhombic structural transition,[23] as noncentrosymmetric crystals are ferroelectric under illumination,[24] which has been observed in $BaTiO_3$.[25] The photoinduced electric field is considered to stabilize the structure itself and trigger local ion migration through/to halide vacancies at the surface,[26,27] thus increasing the PL lifetime and intensity.

The formation of non-centrosymmetric structure in our mixed halide perovskite nanoparticles may be associated with rotation of the MA cations. The $P2_1ma$ space group and their subgroups (e.g. *Pm*) enable the MA cations to independently rotate in the *ac* plane, whereas the MA cations alternate in the *Pnma* space group or $P2_1/m$ (Figure 3e). We consider such rotation of MA cations, probably by the irradiation, is key to form the non-centrosymmetric structures. Our X-ray analysis does not conclusively confirm the rotation of MA cations, however, because carbon and nitrogen atoms are not well recognised by X-ray analysis. Nevertheless, MA cations rotate easily and rapidly (in picoseconds), thereby altering the bandgap[28]; the symmetry lowering is probably correlated with this rotation.[29]

To better understand the impact of symmetry lowering, we performed first-principles calculations of geometrical and electronic structures (Figure S34 and Table S8–12) of three subgroups of $P2_1ma$ with different arrangements of Br and I ions and different ordering of MA cations (alternating or parallel (Figure 3e)). The *Pm* structure with parallel MA cations has a narrower bandgap (~1.7 eV) than structures with alternating MA cations (~1.8 eV) (Figures S35, S36, and Table S10). This ~0.1 eV difference is consistent with the experimental value of 0.2 eV. Furthermore, the structures with parallel MA cations have shorter X–X distances (~3.8 Å) than the structures with alternating MA cations (~4.0 Å) (Table S8), which is in agreement with the PDF result. These simulations indicate that the optical properties of mixed halide perovskites change because of local symmetry lowering, which enables MA cation rotation.

The X-ray structural analysis did not indicate long-range anion ordering as indicated by the site occupancies which correspond to mixed halogen sites (Figure S33); namely, the nanoparticles are considered to be composed of a mosaic of different anion arrangements as simulated by the DFT. Thus, this simulation supports the conclusion that the optical properties are related to local domains in the nanoparticles. The simulation results for possible local domains revealed that lower-symmetry domains have PbX_6 octahedra with shorter Pb–X bonds, as supported by the PDF peak shift for the nearest neighbours (Figure 3c), thus narrowing the bandgap. This structural change is small, but would cause the detectable PL redshift owing to directional charge transfer to the polar domains with smaller band gaps.[30,31]

To conclude, we have proposed a mechanism where the PL redshift originates from symmetry changes between nonpolar and polar systems at the local scale triggered by deformation of PbX_6 octahedra coupled with the rotation of MA cations under light illumination. The local and dynamic symmetry change may not be limited to nanoparticle systems but could also occur at the surface or grain boundaries of perovskite films, leading to anion segregation. This conclusion should be reasonable on the assumption that the structure has the same unit cell as the typical *Pnma* structure and/or is homogeneous, but different interpretation of the experimental data may be possible if the structure is inhomogeneous. Thus, further investigation including verification of polar behavior at the bulk scale is required for concluding more details. Our findings will help to understand the nature of photogenerated polar domains for improving the stability and performance of mixed-halide perovskite solar cells.

ASSOCIATED CONTENT

Supporting Information

Experimental and calculation methods, additional results and discussion. This material is available free of charge via the Internet at http://pubs.acs.org.

AUTHOR INFORMATION

Corresponding Author

* Satoshi Tominaka: TOMINAKA.Satoshi@nims.go.jp
* Takashi Tachikawa: tachikawa@port.kobe-u.ac.jp

Author Contributions

Conceptualization: ST and TT; Sample Preparation: IK and MS; PL Measurements: IK, MS, and TT; Structural Analysis: ST; Synchrotron Experiments: ST, IK, and KO; DFT calculations: TM and TN; Writing – original draft: ST and TT; Writing – review & editing: ST, IK, TM, MS, TN, KO, and TT.

Notes

The authors declare no competing financial interest.

ACKNOWLEDGMENT

We thank Prof. H. Onishi (Kobe University) for his help with the X-ray fluorescence measurements. This work was supported by JSPS KAKENHI (grant Nos. JP18H01944, JP18K05192, JP20H04673 (T.T.)) and the Japan Synchrotron Radiation Research Institute (JASRI) (proposal Nos. 2017A1207, 2018A1304, 2018B2095 (S.T.)).

REFERENCES

(1) Jena, A. K.; Kulkarni, A.; Miyasaka, T. Halide Perovskite Photovoltaics: Background, Status, and Future Prospects. *Chem. Rev.* **2019**, *119* (5), 3036–3103.

(2) Kim, J. Y.; Lee, J.-W.; Jung, H. S.; Shin, H.; Park, N.-G. High-Efficiency Perovskite Solar Cells. *Chem. Rev.* **2020**, *120* (15), 7867–7918.

(3) Dunlap-Shohl, W. A.; Zhou, Y.; Padture, N. P.; Mitzi, D. B. Synthetic Approaches for Halide Perovskite Thin Films. *Chem. Rev.* **2019**, *119* (5), 3193–3295.

(4) McMeekin, D. P.; Sadoughi, G.; Rehman, W.; Eperon, G. E.; Saliba, M.; Horantner, M. T.; Haghighirad, A.; Sakai, N.; Korte, L.; Rech, B.; Johnston, M. B.; Herz, L. M.; Snaith, H. J. A Mixed-Cation Lead Mixed-Halide Perovskite Absorber for Tandem Solar Cells. *Science* **2016**, *351* (6269), 151–155.

(5) Xu, J.; Boyd, C. C.; Yu, Z. J.; Palmstrom, A. F.; Witter, D. J.; Larson, B. W.; France, R. M.; Werner, J.; Harvey, S. P.; Wolf, E. J.; Weigand, W.; Manzoor, S.; van Hest, M. F. A. M.; Berry, J. J.; Luther, J. M.; Holman, Z. C.; McGehee, M. D. Triple-Halide

Wide–Band Gap Perovskites with Suppressed Phase Segregation for Efficient Tandems. *Science* **2020**, *367* (6482), 1097–1104.

(6) Brennan, M. C.; Ruth, A.; Kamat, P. V.; Kuno, M. Photoinduced Anion Segregation in Mixed Halide Perovskites. *Trends Chem.* **2020**, *2* (4), 282–301.

(7) Samu, G. F.; Janaky, C.; Kamat, P. V. A Victim of Halide Ion Segregation. How Light Soaking Affects Solar Cell Performance of Mixed Halide Lead Perovskites. *ACS Energy Lett.* **2017**, *2* (8), 1860–1861.

(8) Tang, X.; van den Berg, M.; Gu, E.; Horneber, A.; Matt, G. J.; Osvet, A.; Meixner, A. J.; Zhang, D.; Brabec, C. J. Local Observation of Phase Segregation in Mixed-Halide Perovskite. *Nano Lett.* **2018**, *18* (3), 2172–2178.

(9) Mao, W.; Hall, C. R.; Bernardi, S.; Cheng, Y.-B.; Widmer-Cooper, A.; Smith, T. A.; Bach, U. Light-Induced Reversal of Ion Segregation in Mixed-Halide Perovskites. *Nat. Mater.* **2021**, *20* (1), 55–61.

(10) Hoke, E. T.; Slotcavage, D. J.; Dohner, E. R.; Bowring, A. R.; Karunadasa, H. I.; McGehee, M. D. Reversible Photo-Induced Trap Formation in Mixed-Halide Hybrid Perovskites for Photovoltaics. *Chem. Sci.* **2015**, *6* (1), 613–617.

(11) Draguta, S.; Sharia, O.; Yoon, S. J.; Brennan, M. C.; Morozov, Y. V; Manser, J. M.; Kamat, P. V; Schneider, W. F.; Kuno, M. Rationalizing the Light-Induced Phase Separation of Mixed Halide Organic-Inorganic Perovskites. *Nat. Commun.* **2017**, *8*, 200.

(12) Mosconi, E.; Meggiolaro, D.; Snaith, H. J.; Stranks, S. D.; De Angelis, F. Light-Induced Annihilation of Frenkel Defects in Organo-Lead Halide Perovskites. *Energy Environ. Sci.* **2016**, *9* (10), 3180–3187.

(13) Jang, D. M.; Park, K.; Kim, D. H.; Park, J.; Shojaei, F.; Kang, H. S.; Ahn, J. P.; Lee, J. W.; Song, J. K. Reversible Halide Exchange Reaction of Organometal Trihalide Perovskite Colloidal Nanocrystals for Full-Range Band Gap Tuning. *Nano Lett.* **2015**, *15* (8), 5191–5199.

(14) Tachikawa, T.; Karimata, I.; Kobori, Y. Surface Charge Trapping in Organolead Halide Perovskites Explored by Single-Particle Photoluminescence Imaging. *J. Phys. Chem. Lett.* **2015**, *6* (16), 3195–3201.

(15) Galland, C.; Ghosh, Y.; Steinbrück, A.; Sykora, M.; Hollingsworth, J. A.; Klimov, V. I.; Htoon, H. Two Types of Luminescence Blinking Revealed by Spectroelectrochemistry of Single Quantum Dots. *Nature* **2011**, *479* (7372), 203–207.

(16) Brennan, M. C.; Draguta, S.; Kamat, P. V.; Kuno, M. Light-Induced Anion Phase Segregation in Mixed Halide Perovskites. *ACS Energy Lett.* **2018**, *3* (1), 204–213.

(17) Belisle, R. A.; Bush, K. A.; Bertoluzzi, L.; Gold-Parker, A.; Toney, M. F.; McGehee, M. D. Impact of Surfaces on Photoinduced Halide Segregation in Mixed-Halide Perovskites. *ACS Energy Lett.* **2018**, *3* (11), 2694–2700.

(18) Glazer, A. M. The Classification of Tilted Octahedra in Perovskites. *Acta Crystallogr. Sect. B-Structural Sci.* **1972**, *B 28*, 3384–3391.

(19) Page, K.; Siewenie, J. E.; Quadrelli, P.; Malavasi, L. Short-Range Order of Methylammonium and Persistence of Distortion at the Local Scale in $MAPbBr_3$ Hybrid Perovskite. *Angew. Chem. Int. Ed.* **2016**, *55* (46), 14318–14322.

(20) Laurita, G.; Fabini, D. H.; Stoumpos, C. C.; Kanatzidis, M. G.; Seshadri, R. Chemical Tuning of Dynamic Cation Off-Centering in the Cubic Phases of Hybrid Tin and Lead Halide Perovskites. *Chem. Sci.* **2017**, *8* (8), 5628–5635.

(21) Yang, Y.; Ren, W.; Stengel, M.; Yan, X. H.; Bellaiche, L. Revisiting Properties of Ferroelectric and Multiferroic Thin Films under Tensile Strain from First Principles. *Phys. Rev. Lett.* **2012**, *109* (5), 057602.

(22) Song, G.; Gao, B. L.; Li, G. N.; Zhang, J. First-Principles Study on the Electric Structure and Ferroelectricity in Epitaxial $CsSnI_3$ Films. *Rsc Adv.* **2017**, *7* (65), 41077–41083.

(23) Moriwake, H.; Kuwabara, A.; Fisher, C. A. J.; Taniguchi, H.; Itoh, M.; Tanaka, I. First-Principles Calculations of Lattice Dynamics in $CdTiO_3$ and $CaTiO_3$: Phase Stability and Ferroelectricity. *Phys. Rev. B* **2011**, *84* (10), 104114.

(24) Von Baltz, R.; Kraut, W. *Theory of the Bulk Photovoltaic Effect in Pure Crystals*; 1981; Vol. 28.

(25) Young, S. M.; Rappe, A. M. First Principles Calculation of the Shift Current Photovoltaic Effect in Ferroelectrics. *Phys. Rev. Lett.* **2012**, *109* (11), 116601.

(26) Bischak, C. G.; Wong, A. B.; Lin, E.; Limmer, D. T.; Yang, P.; Ginsberg, N. S. Tunable Polaron Distortions Control the Extent of Halide Demixing in Lead Halide Perovskites. *J. Phys. Chem. Lett.* **2018**, *9* (14), 3998–4005.

(27) Zhang, H.; Fu, X.; Tang, Y.; Wang, H.; Zhang, C.; Yu, W. W.; Wang, X.; Zhang, Y.; Xiao, M. Phase Segregation Due to Ion Migration in All-Inorganic Mixed-Halide Perovskite Nanocrystals. *Nat. Commun.* **2019**, *10*, 1088.

(28) Mehdizadeh, A.; Akhtarianfar, S. F.; Shojaei, S. Role of Methylammonium Rotation in Hybrid Halide $MAPbX_3$ (X = I, Br, and Cl) Perovskites by a Density Functional Theory Approach: Optical and Electronic Properties. *J. Phys. Chem. C* **2019**, *123* (11), 6725–6734.

(29) Beecheri, A. N.; Semonin, O. E.; Skelton, J. M.; Frost, J. M.; Terban, M. W.; Zhai, H.; Alatas, A.; Owen, J. S.; Walsh, A.; Billinge, S. J. L. L.; Beecher, A. N.; Semonin, O. E.; Skelton, J. M.; Frost, J. M.; Terban, M. W.; Zhai, H.; Alatas, A.; Owen, J. S.; Walsh, A.; Billinge, S. J. L. L. Direct Observation of Dynamic Symmetry Breaking above Room Temperature in Methylammonium Lead Iodide Perovskite. *Acs Energy Lett.* **2016**, *1* (4), 880–887.

(30) Karimata, I.; Kobori, Y.; Tachikawa, T. Direct Observation of Charge Collection at Nanometer-Scale Iodide-Rich Perovskites during Halide Exchange Reaction on $CH_3NH_3PbBr_3$. *J. Phys. Chem. Lett.* **2017**, *8* (8), 1724–1728.

(31) Karimata, I.; Ohta, K.; Kobori, Y.; Tachikawa, T. Several Orders of Magnitude Difference in Charge-Transfer Kinetics Induced by Localized Trapped Charges on Mixed-Halide Perovskites. *ACS Appl. Mater. Interfaces* **2018**, *10* (43), 37057–37066.

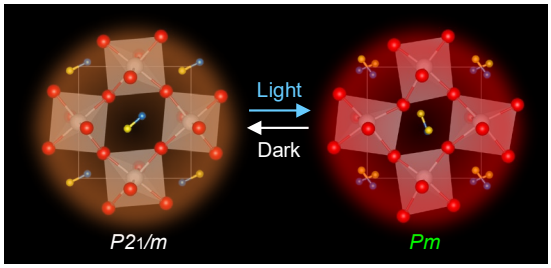
Light
Dark
P2₁/m
Pm